applied optics

Subwavelength Bessel beam arrays with high uniformity based on a metasurface

CHENYANG WU,[1,2] XUANLUN HUANG,[1,2] JI YIPENG,[2] JIAXING WANG,[2] AND CONNIE J. CHANG-HASNAIN[1,2,3,4,*]

[1]School of Information Science and Technology, Fudan University, Shanghai 200433, China
[2]Berxel Photonics Co. Ltd., Shenzhen 518071, China
[3]Chinese University of Hong Kong, Shenzhen 518172, China
[4]Peng Cheng Laboratory, Shenzhen 518055, China
*connie.chang@berxel.com

Received 23 January 2024; revised 22 February 2024; accepted 22 February 2024; posted 23 February 2024; published 13 March 2024

Bessel beam arrays are highly attractive due to non-diffraction properties, parallel processing, and large capacity capabilities. However, conventional approaches of generating Bessel beams, such as spatial light modulators, axicons, and diffraction optical elements, suffer from various limitations of system complexity and bulkiness, low uniformity, and limited numerical aperture (NA). The limited NA imposes constraints on achieving minimal full width at half maximum (FWHM) of the Bessel beam, ultimately compromising the resolution of the beam. In this study, we demonstrate a method for generating Bessel beam arrays with regular and random patterns via an ultra-compact metasurface. This approach integrates the phase profile of an optimized beam splitter with a meta-axicon. The Bessel beam arrays exhibit subwavelength dimensions of FWHM (590 nm, ∼0.9λ) and relatively high uniformity of 90% for NA = 0.2 and 69% for NA = 0.4. Furthermore, the method achieves effective suppression of background noise and zeroth-order intensity compared to methods based on Dammann grating (DG) based metasurfaces. The proposed method highlights potential applications of Bessel beam arrays in various fields, such as laser machining, optical communication, and biomedical imaging.

https://doi.org/10.1364/AO.519840

1. INTRODUCTION

Bessel beams were discovered in the 1980s by Durin while solving the free-space Helmholtz equation [1], and have since garnered widespread attention due to unique properties, such as non-diffraction and self-reconstruction [1,2]. Unlike conventional Gaussian beams, non-diffracting properties allow them to maintain the shape and intensity profile over a longer distance. Bessel beams also have self-reconstruction properties, which can reform the shape after encountering obstacles. Furthermore, Bessel beams have smaller beam waists than Gaussian beams, which leads to higher spatial resolution and reduced scattering. In particular, Bessel beam arrays composed of multiple Bessel beams have parallel processing and large capacity capabilities. To date, Bessel beams have proven to be valuable tools in a wide range of applications, such as photolithography and laser processing [3], microscopy imaging [4], biomedical applications [5], particle trapping [6], and radar and LiDAR imaging [7,8].

Conventional methods for generating Bessel beams, such as axicons [9], spatial light modulators (SLMs) [10,11], 3D phase plates [12], holographic screens [13], diffractive optical elements [14], and computer-generated holograms [15], suffer from various limitations such as system complexity and bulkiness, low beam uniformity and efficiency, limited depth of focus (DOF) and NA, which have severely impeded the efficient integration and miniaturization of optical devices. For example, when employing the SLM to generate a Bessel beam array, the SLM needs to be divided into subregions that can provide multiple axicon phase distributions, and the objective lens must be precisely paired with an annular aperture [16]. However, this approach suffers from poor imaging efficiency. Moreover, the energy distribution in the array can exhibit drastic reduction of uniformity, and in the event of any mismatch between the objective lens and aperture will result in a significant deterioration of the array pattern.

Metasurfaces, consisting of artificially engineered ultra-thin planar structures with subwavelength feature sizes, have attracted significant attention in recent years due to the ability to precisely control the phase, polarization, amplitude, and frequency of incident electromagnetic waves at subwavelength scales [17–19], driving the development of ultra-compact nano-photonics systems. Nano-coding technology based on metasurfaces has provided a new design approach for the ultra-thin, miniaturized, and device integration of Bessel beams. In terms of single Bessel beam generation, Chen *et al.* generated meta-axicons with a high numerical aperture by using TiO_2

nano-fins with height of 600 nm, capable of producing Bessel beams with different orders [20]. However, the high aspect ratio (10:1) presented the challenge for large-scale micro-nano fabrication. Wang *et al.* efficiently generated non-diffracting Bessel beams by using a single-layer and grounded dielectric substrate with a metallic patch consisting of a square and a ring part [21]. Nevertheless, the unit-cell period was 15.68 mm and only worked in the 5.8 GHz frequency band. Other techniques such as dielectric meta-walls [22], plasmonic metasurfaces [23], and catenary nanostructures [24] have also been employed to generate Bessel beams, yet face problems of low efficiency and uniformity.

Based on the theoretical and experimental research of single Bessel beams, researchers have further explored generating Bessel beam arrays using metasurfaces. Chen *et al.* proposed a multifocal axicon metalens to generate the Bessel beam array by placing four nano-pillars of different sizes and rotational directions (maximum aspect ratio of 9:1) within a single unit cell, achieving a 2×2 Bessel beam array [25]. However, increasing the number of focal spots is quite challenging for fabrication, as it requires adding more nano-pillar structures within a single unit cell. To increase the density and uniformity of focal spots, researchers have considered utilizing Dammann gratings (DGs) in generating Bessel beam arrays. Lin *et al.* integrated the phase-mask function of DGs and axicons, and utilized Huygens metasurfaces composed of cylinder nano-posts to achieve the 5×5 Bessel beam array at a wavelength of 780 nm [26]. Nevertheless, this method is unable to produce subwavelength Bessel beams, with low NA of 0.0195 and full width at half maximum (FWHM) of approximately 1600 nm, and the much higher zeroth-order intensity results in poor beam uniformity of 42.15%. Chen *et al.* improved the uniformity of Bessel beam arrays by optimizing the unit-cell size of DGs, achieving relatively high uniformity (approximately 52%) at $\mathrm{NA} = 0.4$, thus improving the resolution and imaging quality of the array at subwavelength scales [27]. The uniformity and high spatial resolution of Bessel beam arrays are critically important for various applications including optical lithography, laser processing, optical manipulation, and microscopy imaging. Therefore, achieving ultra-thinness, high uniformity, and device integration of Bessel beam arrays is a significant and urgent task.

In this study, we demonstrate a novel method to enhance the uniformity of Bessel beam arrays using an ultra-compact Pancharatnam–Berry (PB) phase metasurface. This approach integrates the phase profile of an optimized beam splitter with a meta-axicon. The illustration diagram of the proposed nanostructure all-dielectric metasurface is shown in Fig. 1. Leveraging the known symmetry properties of the Bessel array, we enhance uniformity and average intensity through optimization and restriction of the initial random phase and updated recovery phase during the iteration process. Based on metasurfaces of silicon nanopillars on glass substrate, we implement the generation of a Bessel beam array with a 4×4 regular pattern, and triangular and random patterns. These arrays exhibit subwavelength dimensions of FWHM (590 nm, $\sim 0.9\lambda$) and relatively high uniformity of 90% for $\mathrm{NA} = 0.2$ and 69% for $\mathrm{NA} = 0.4$. Importantly, our method achieves effective suppression of background noise and zeroth-order intensity compared to methods based on Dammann grating (DG) based metasurfaces.

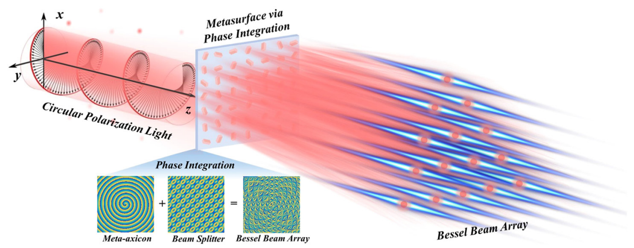

Fig. 1. Illustration of the proposed metasurface via phase integration for Bessel beam array.

Furthermore, by incorporating a compensation phase from a Gaussian light source, we enable the focusing of the VCSEL incident beam onto the metasurface through phase control, eliminating the need for a conventional collimating lens. This facilitates ultra-compact monolithic integration with commercial VCSELs. We anticipate that our proposed method will shed light on the potential applications of Bessel beam arrays across diverse fields. From laser machining, optical alignment, and optical communication to biomedical imaging and multiplex imaging, the ultra-compactness, enhanced uniformity, and resolution offered by our methodology open new avenues for exploration and innovation.

2. PHASE PROFILE DESIGN AND GENERATION OF BESSEL BEAM ARRAY

Bessel beams are a particular class of solutions to the free space Helmholtz wave equation, which exhibit non-diffraction behavior along the z-axis. The field distribution of Bessel beams in this direction can be mathematically expressed using cylindrical coordinates (r, φ, z), where the intensity profile is characterized by the Bessel functions of the first kind:

$$E(r, \varphi, z) = A \cdot \exp(i k_z) \cdot J_n(k_r), \tag{1}$$

assuming that A is the amplitude of the field, and k_z and k_r are the longitudinal and transverse wave vectors, respectively, which satisfy the equation $\sqrt{k_z^2 + k_r^2} = k$, where k is the wave vector. According to Eq. (1), Bessel beams have transverse intensity profiles independent of the z coordinate, resulting in non-diffraction properties. The ideal Bessel beam carries infinite energy, while in practical approximations, an axicon phase is utilized to achieve the generation of zeroth- order Bessel beams. The phase profile of the meta-axicon for generating zeroth-order Bessel beams can be expressed as

$$\varphi(x, y) = 2\pi - \frac{2\pi}{\lambda_d} \cdot \sqrt{x^2 + y^2} \cdot \mathrm{NA}, \tag{2}$$

where λ_d is the wavelength of the light, NA is the numerical aperture, and $\sqrt{x^2 + y^2} = r$ (r is the radial coordinate). In order to generate the high-order Bessel beams, we need to add a term of azimuthal angle $\Phi = \mathrm{atan}(y/x)$, which represents the vortex phase, accordingly expressed as

$$\varphi(x, y) = 2\pi - \frac{2\pi}{\lambda_d} \cdot \sqrt{x^2 + y^2} \cdot \mathrm{NA} + n\Phi, \tag{3}$$

where n is the topological charge number (the order of Bessel beams).

In this study, we integrate the phase profile of a meta-axicon with a beam splitter via an optimized phase retrieval algorithm based on the iterative Fourier transform algorithm (IFTA) to generate Bessel beam arrays with enhanced uniformity. IFTA is a representative class of iterative methods for phase retrieval that can generate pure phase holograms. One of its distinguishing features is the recursive Fourier transform and updating process that iterates between two planes. Gerchberg and Saxton utilized it for phase extraction [28] and afterwards it became the most widely used method in the field of iterative holography algorithms. The IFTA algorithm is based on the principle of iterative amplitude and phase retrieval by enforcing the constraints of amplitude and phase in both Fourier domains until a satisfactory solution is reached. This algorithm iteratively propagates the input field to the output plane by Fourier transform, adjusts the amplitude and phase constraints in the Fourier domain, and then propagates the modified field back to the input plane. This process is repeated until convergence is achieved.

Next, the in-depth analysis of the process to design a diffractive optical element (DOE) that yields the desired intensity distribution in the focal plane will be conducted. The following equation mathematically represents the complex amplitude of the input light field $I(x, y)$ of the phase-only DOE:

$$I(x, y) = E_{\text{in}}(x, y) \exp\left[i\varphi(x, y)\right], \tag{4}$$

in which $E_{\text{in}}(x, y)$ denotes the complex amplitude of the incident light and $\exp[i\varphi(x, y)]$ is the transmission function of the DOE with phase distribution $\varphi(x, y)$. Similarly, the complex amplitude $F(x', y')$ of the output light field in the focal plane is presented as

$$\begin{aligned} F\left(x', y'\right) &= O\left(x', y'\right) \exp\left[i\psi\left(x', y'\right)\right] \\ &= \frac{ik}{2\pi f} \exp(ikf) \iint_{-\infty}^{\infty} I(x, y) \\ &\quad \times \exp\left[ik\left(xx' + yy'\right)\right] \mathrm{d}x\mathrm{d}y, \end{aligned} \tag{5}$$

where $O(x', y')$ and $\psi(x', y')$ represent the desired amplitude and phase distribution in the output focal plane, respectively, and k is the wave vector ($k = 2\pi/\lambda$). Accordingly, the desired target intensity distribution in the focal plane $I_0(x', y')$ is expressed as

$$I_0(x', y') = \left|F(x', y')\right|^2 = \left|O(x', y')\right|^2. \tag{6}$$

Therefore, solving the equation above is a requisite step towards designing the phase profile of the DOE.

In the process of solving the integral equation via IFTA, an initial random phase is required as an input, and the phase is iteratively inferred based on the reconstructed target amplitude. Therefore, the selection of the initial phase can drastically affect the convergence speed and accuracy of the algorithm. In this study, we combine the phase profile of a beam splitter with a meta-axicon to realize the generation of Bessel beam arrays. The objective of the beam splitter phase is to implement the regular Bessel beam array with uniform intensity and central symmetry features in the focal plane. Consequently, we propose an improved optimization and restriction method for both the initial and iterative updating phases by leveraging the prior information of the symmetry property of the Bessel beam array target distribution. This approach can expedite the algorithm convergence and enhance the accuracy of the recovered phase in comparison with conventional random iterative phase. The proposed optimized phase retrieval algorithm based on modified IFTA (MIFTA) for generating uniform and symmetry intensity distribution is as follows.

Step 1. Set initial input phase $\varphi_i(x, y)$ randomly from 0 to 2π with iteration number of i, and reset the initial input phase $\varphi_i'(x, y) = \varphi_{i\_\text{tri}}(x, y) + \varphi_{i\_\text{tri}}(x, y)^T$, where $\varphi_{i\_\text{tril}}(x, y)$ is the lower or upper triangular portion of $\varphi_i(x, y)$, and $\varphi_{i\_\text{tri}}(x, y)^T$ is the corresponding transposed matrix.

Step 2. Utilize the fast Fourier transform to calculate the complex amplitude $F_i(x', y')$ of the focal plane in Eq. (5).

Step 3. Replace the amplitude of calculated $F_i(x', y')$ with desired amplitude distribution $O(x', y')$ and reset the complex amplitude as $F_i'(x', y') = O(x', y') \cdot F_i(x', y')/|F_i(x', y')|$.

Step 4. Utilize the inverse fast Fourier transform to calculate the updated complex amplitude $I_{i+1}'(x, y)$ of the input DOE plane in Eq. (6), and calculate the corresponding DOE phase $\varphi_{i+1}'(x, y) = \arg[I_{i+1}'(x, y)]$.

Step 5. Reset the calculated estimated phase $\varphi_{i+1}'(x, y) = \varphi_{i+1\_\text{tri}}'(x, y) + \varphi_{i+1\_\text{tri}}'(x, y)^T$.

Step 6. Calculate the amplitude distribution error with respect to the desired amplitude distribution by $e_i = |O^2(x', y') - F_i^2(x', y')|$.

Step 7. Determine whether e_i and iteration number i have reached the setting threshold; if so, terminate the algorithm to obtain the reconstructed beam splitter phase profile. Otherwise, return to Step 2 and repeat the iteration process.

We set a desired target intensity distribution that consists of a 4×4 uniform dot array as illustrated in Fig. 2(a) to verify the feasibility of the proposed algorithm. The phase reconstruction is performed using both IFTA and MIFTA with 200 iterations to calculate the reconstructed intensity distribution in the focal plane. By exploiting the symmetry of the target intensity distribution as prior information, the MIFTA method imposes constraints on the phase updates to enforce diagonal symmetry during the iterations, which enhances the reconstruction performance in terms of a higher probability of obtaining superior reconstruction results. The variations of the average intensity and non-uniformity of the reconstructed target array with respect to the iteration number are shown in Fig. 2(b) and Fig. 2(c), respectively. The non-uniformity is defined as $[\max(I_n) - \min(I_n)\max(I_n) + \min(I_n)]$, where I_n is the intensity of the reconstructed target array, and $\max(I_n)$ and $\min(I_n)$ are the maximum and minimum intensity among all the target, respectively. The converged average intensities and non-uniformity of the reconstructed target array via IFTA and MIFTA are 0.949/0.0569 and 0.9922/0.0076, respectively. The simulation results indicate that MIFTA outperforms IFTA in terms of reconstruction accuracy, while the convergence speed is slightly slower. It is worth noting that the randomness of the initial phase will result in different upper limits of reconstruction accuracy for two different algorithms, so it is indispensable to repeat the entire iterative process multiple times to obtain the optimal phase reconstruction result.

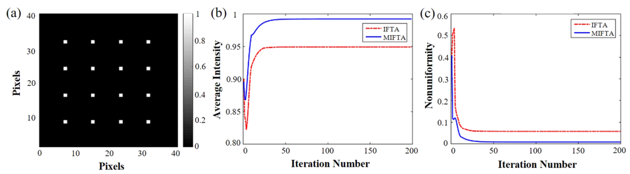

Fig. 2. Comparison of IFTA and MIFTA calculation methods. (a) Desired target intensity distribution. (b), (c) Average intensity and nonuniformity of reconstructed target array via IFTA and MIFTA, respectively.

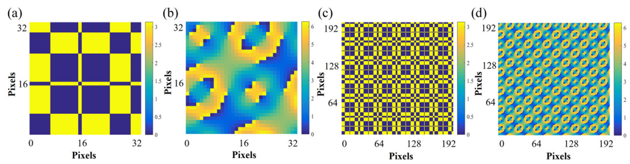

Fig. 3. Phase distribution of 4×4 beam splitter corresponding to DG and MIFTA calculation methods. (a), (b) Phase distribution unit calculated via DG and MIFTA, respectively. (c), (d) Extended phase distribution calculated via DG and MIFTA, respectively.

Additionally, we can further flexibly extend the application scope and approach of the proposed algorithm, which fundamentally relies on the practical prior information of target features. For instance, if the target distribution exhibits a sparsity feature as prior information, classical imaging reconstruction algorithms for compressive sensing, such as the orthogonal matching pursuit (OMP) [29] algorithm and complex approximated message passing (CAMP) [30] algorithm, can be considered and incorporated into the phase retrieval algorithm to further enhance the accuracy of reconstruction results. Here, we refrain from extensively elaborating on the expanded algorithm, which is beyond the main scope of this study.

We calculate the optimized phase distribution of the beam splitter via MIFTA as shown in Fig. 3(b), which can generate a 4×4 Bessel beam array in the focal plane. As a comparison, phase distribution of the 4×4 beam splitter using a conventional $(0, \pi)$ binary DG [31] is also designed, as shown in Fig. 3(a). The phase distributions of the beam splitter are extended periodically as shown in Figs. 3(c) and 3(d), corresponding to DG and the proposed MIFTA calculation methods.

By integrating the calculated phase profile of the beam splitter $\varphi_{\mathrm{bs}}(x, y)$ with the meta-axicon for generating Bessel beams in Eq. (3), the total phase profile for generating the Bessel beam array is derived as

$$\varphi_{\mathrm{total}}(x, y) = 2\pi - \frac{2\pi}{\lambda_d} \cdot \sqrt{x^2 + y^2} \cdot \mathrm{NA} + n\Phi + \varphi_{\mathrm{bs}}(x, y). \quad \textbf{(7)}$$

Based on the above equation, the total phase distribution for generating a 4×4 zeroth-order Bessel beam array utilizing DG and MIFTA methods is calculated. When $\mathrm{NA} = 0.2$, the total phase distributions based on DG and MIFTA methods are shown in Fig. 4(a) and Fig. 4(b), respectively. Similarly, when $\mathrm{NA} = 0.4$, the total phase distributions of the two methods are shown in Figs. 4(c) and 4(d).

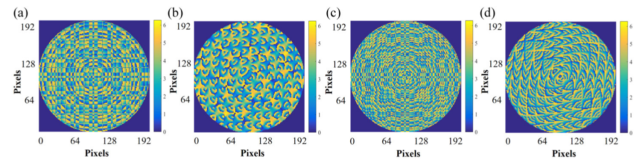

Fig. 4. Total phase distribution for generating 4×4 zero-order Bessel beam corresponding to DG and MIFTA calculation methods. (a), (b) Total phase distribution calculated via DG and MIFTA with $\mathrm{NA} = 0.2$, respectively. (c), (d) Total phase distribution calculated via DG and MIFTA with $\mathrm{NA} = 0.4$, respectively.

Moreover, by adding the compensation phase term of the Gaussian light source, the emitted light of VCSEL can be focused onto the metasurface through phase control without the need for a conventional collimating lens, so as to realize the ultra-compact monolithic integration with commercial VCSELs [32]. The total phase profile for generating Bessel beam arrays with a compensation phase for a VCSEL source is denoted as

$$\varphi'_{\mathrm{total}}(x, y) = \varphi_{\mathrm{total}}(x, y) + \varphi_{\mathrm{compensation}}(x, y), \quad \textbf{(8)}$$

where $\varphi_{\mathrm{compensation}}(x, y) = k(x^2 + y^2)/(2R(z))$, in which $k = n_1 \frac{2\pi}{\lambda}$ is the wavenumber of the VCSEL source in the substrate material, n_1 is the refractive index of the substrate material, λ is the wavelength of the VCSEL source, and $R(z)$ is the curvature radius of the VCSEL source emitting on the surface of the substrate.

3. DESIGN OF PB PHASE BASED METASURFACE FOR BESSEL BEAM ARRAYS

In this section, we utilize the calculated total phase distribution from the above section, to implement the encoding of the PB phase based metasurface. The diagram of the unit cell is illustrated in Fig. 5(a), which consists of a single-layer amorphous silicon cuboid nanorod with the rotation angle θ placed on the fused silica substrate. According to the basic principle of PB phase [33], the total phase distribution $\varphi_{\mathrm{total}}(x, y)$ can be encoded by phase modulation utilizing nanorods with the same length (L), width (W), and height (H) with diverse rotation angles $\theta(x, y)$. For example, when the incident light is left-handed circular polarization (LCP), the PB phase metasurface can modulate the phase by adjusting the rotation angle $\theta(x, y)$ of the nanorods to generate right-handed circular polarization (RCP) light with a geometric phase $\varphi(x, y)$, where $\theta(x, y) = 1/2 \cdot \varphi(x, y)$. Thus, the rotation angle $\theta(x, y)$ of the nanorods in the range of 0°–180°on the incident plane corresponds to the transmitted geometric phase $\varphi(x, y)$ in the range of 0–360° on the output plane. The lattice constant $\mathrm{P} = 250$ nm, and a set of geometric parameters with high polarization conversion efficiency, including $\mathrm{H} = 300$ nm, $\mathrm{L} = 135$ nm, and $\mathrm{W} = 85$ nm, is chosen for incident light with 630 nm wavelength. Based on the total phase distribution for generating the 4×4 Bessel beam array via DG and MIFTA methods shown in Fig. 4, the parameters of the metasurface are calculated utilizing phase-to-rotation-angle conversion encoding. The top view of a portion of the designed metasurface is shown in Fig. 5(b). Regarding the fabrication process, the

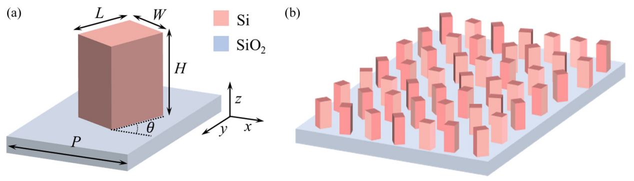

Fig. 5. (a) Unit cell of the proposed metasurface and (b) schematic diagram of the designed metasurface, which consists of single-layer array of amorphous silicon nanorods placed on the fused silica substrate with same length L, width W, and height H while diverse rotation angles θ.

designed metasurface can be fabricated using conventional electron beam lithography (EBL) coupled with an etching process, thereby validating the practicality and viability of the proposed method. In practical applications, a prevalent method to generate circularly polarized light involves manipulating a collimated beam from a conventional laser source. This can be achieved by combining a linear polarizer with a quarter-wave plate. By orienting the quarter-wave plate at a 45° angle with respect to the polarization direction of the linear polarizer, a circularly polarized beam can be generated. Subsequently, this incident light can be used to perpendicularly illuminate the metasurface.

Finite difference time domain (FDTD) software (Lumerical Inc.) is used to calculate the light field intensity distributions of the Bessel beam array based on DG and MIFTA methods with NA = 0.2 and 0.4, which are shown in Fig. 6 and Fig. 7, respectively. For NA = 0.2, Figs. 6(a) and 6(c) present the transverse intensity distributions in the x-y plane corresponding to DG and MIFTA methods, respectively, whereas Figs. 6(b) and 6(d) present the longitudinal intensity distributions in the x-z plane of the two methods. The theoretical calculation formula for the depth of focus (DoF) of the zeroth-order Bessel beam is given by DoF = $D/2\tan(\mathrm{asin}(\mathrm{NA}))$, where D is the diameter of the metasurface. It can be derived that the non-diffraction propagation distance can be increased by enlarging the size of the metasurface and decreasing NA. For NA = 0.2, the theoretical DoF is calculated to be 117.58 μm, and the experimental DoFs corresponding to DG and MIFTA methods are 115 μm and 117 μm, respectively, which are in good agreement with theoretical values. Furthermore, the intensity profiles at the position of white dashed lines in Figs. 6(b) and 6(d) are extracted and plotted in Figs. 8(a) and 8(b). The calculated nonuniformities for DG and MIFTA methods are 0.1479 and 0.0999, respectively. The MIFTA method exhibits better suppression of background noise and central zeroth-order intensity with higher uniformity, resulting in better imaging quality. For a zeroth-order Bessel beam, the theoretical value of FWHM is given by FWHM = $2.25/k_r = 1.13$ μm, where $k_r = 2\pi \cdot \mathrm{NA}/\lambda$ [20], and the experimental FWHMs corresponding to DG and MIFTA methods are approximately 1.11 μm and 1.10 μm, respectively.

Similarly, when NA = 0.4, Figs. 7(a) and 7(c) present the transverse intensity distributions in the x-y plane corresponding to DG and MIFTA methods, respectively, whereas Figs. 7(b) and 7(d) present the longitudinal intensity distributions in the x-z plane. The theoretical value of DoF is 54.99 μm with NA = 0.4, and the experimental DoFs corresponding to DG and MIFTA methods are 48 μm and 53 μm, respectively,

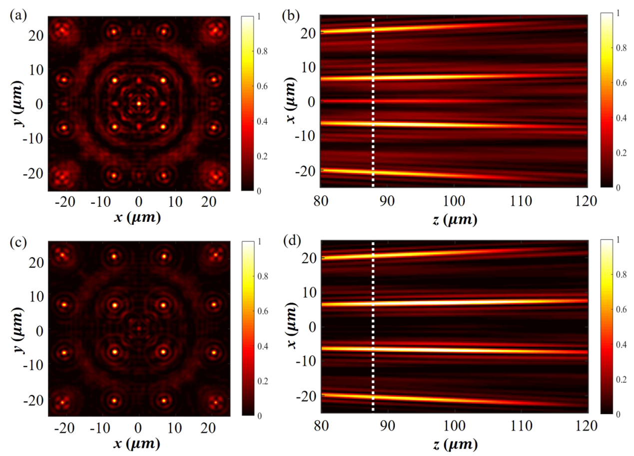

Fig. 6. Intensity distributions of the Bessel beam array based on the DG and MIFTA methods with NA = 0.2. Transverse intensity distributions in x-y plane corresponding to (a) DG and (c) MIFTA methods. Longitudinal intensity distributions in x-z plane corresponding to (b) DG and (d) MIFTA methods.

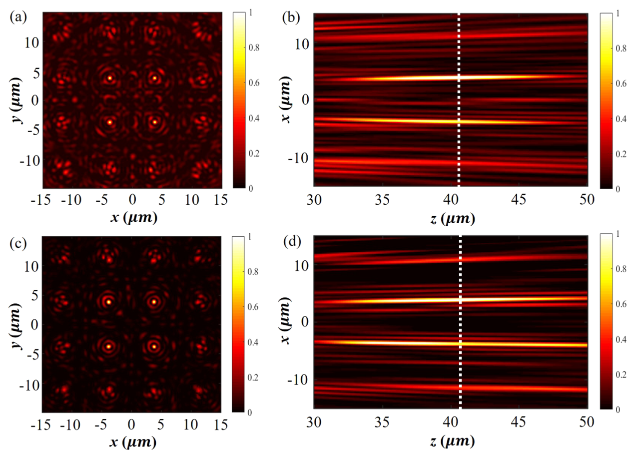

Fig. 7. Intensity distributions of the Bessel beam array based on the DG and MIFTA methods with NA = 0.4. Transverse intensity distributions in x-y plane corresponding to (a) DG and (c) MIFTA methods. Longitudinal intensity distributions in x-z plane corresponding to (b) DG and (d) MIFTA methods.

which are reasonably close to the theoretical value. Moreover, the intensity profiles at the position of white dashed lines in Figs. 7(b) and 7(d) are extracted and plotted in Figs. 8(c) and 8(d), and the calculated nonuniformities for DG and MIFTA are 0.4922 and 0.3072. Additionally, the theoretical FWHM for NA = 0.4 is 0.565 μm, and the experimental FWHMs corresponding to DG and MIFTA methods are approximately 0.5686 μm and 0.5897 μm, respectively.

It is noteworthy that the increasement of NA from 0.2 to 0.4 results in distortion at the edges of the Bessel beam array, leading to a significant decrease in imaging quality due to the imprecision of the beam splitter phase resulting from the limited number of nanorods within a single period. The imaging quality under high NA conditions can be improved by appropriately increasing the number of nanorods within a single period, i.e., increasing the period size. Utilizing the similar approach,

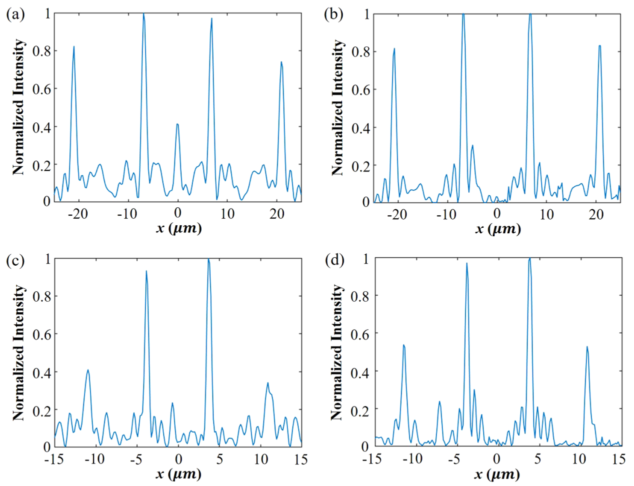

Fig. 8. Intensity cross profiles with NA = 0.2 corresponding to (a) DG and (b) MIFTA methods; and NA = 0.4 corresponding to (c) DG and (d) MIFTA methods.

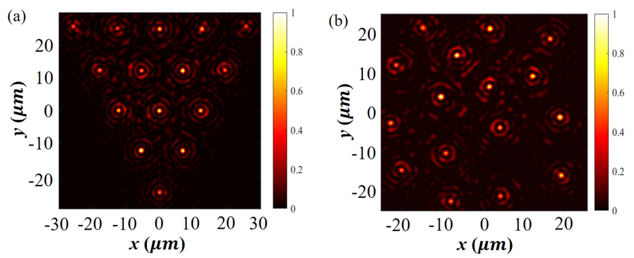

Fig. 9. Light field transverse intensity distributions of the Bessel beam array in the x-y plane with (a) triangular pattern and (b) random pattern.

light field intensity distributions of the Bessel beam array in the x-y plane with a triangular pattern and random pattern are shown in Fig. 9. In general, theoretical analyses and experimental results demonstrate good agreement, and the proposed method shows superior performance in evaluation aspects such as DoF, uniformity, as well as suppression of background noise and central zeroth-order intensity. Table 1 summarizes the comparison of this work and previous related work for Bessel beam array generation based on metasurfaces, and shows the superiority of our work including the maximum aspect ratio of the metasurface unit, subwavelength dimension of FWHM, and uniformity.

4. CONCLUSION

In this study, we proposed a novel method for generating enhanced uniformity of a non-diffraction 4×4 Bessel beam array as well as triangular and random pattern arrays via an ultra-thin and compact metasurface using the MIFTA phase retrieval method. Simulation results verified the effectiveness with a subwavelength dimension of FWHM (590 nm, $\sim 0.9\lambda$) and relatively high uniformity of 90% for NA = 0.2 and 69% for NA = 0.4 of Bessel beam arrays, which demonstrate good agreement with theoretical analysis. The proposed method presents superior performance in evaluation aspects such as DoF, uniformity of beam arrays, suppression of background noise, and central zeroth-order intensity compared to the DG based method. The proposed method has potential for widespread applications in the field of non-diffractive beam array generation with ultra-thin and compact characteristics and suitability for high integration, promoting miniaturization and multifunctionality of optoelectronic devices and systems.

Funding. Hetao Shenzhen-Hong Kong Science and Technology Innovation Cooperation Zone Program (HZQSWS-KCCYB-202203); Shenzhen Science and Technology Innovation Program (JSGG20220831110404008, KQTD20200820113053102, ZDSYS20220325163600001); Guangdong Major Talent Introduction Project (2021ZT09X328).

Disclosures. The authors declare no conflicts of interest.

Data availability. Data underlying the results presented in this paper are not publicly available at this time but may be obtained from the authors upon reasonable request.

REFERENCES

1. J. Durnin, "Exact solutions for nondiffracting beams. I. The scalar theory," J. Opt. Soc. Am. A **4**, 651–654 (1987).
2. Z. Bouchal, J. Wagner, and M. Chlup, "Self-reconstruction of a distorted nondiffracting beam," Opt. Commun. **151**, 207–211 (1998).
3. X. Li, Z. Xu, L. Jiang, *et al.*, "Creating a three-dimensional surface with antireflective properties by using femtosecond-laser Bessel-beam-assisted thermal oxidation," Opt. Lett. **45**, 2989–2992 (2020).
4. S. Li, J. Jiao, J. Boonruangkan, *et al.*, "Self-reconstructing Bessel beam created by two-photon-polymerized micro-axicon for light-sheet fluorescence microscopy," Results Phys. **24**, 104111 (2021).
5. Y. Ren, H. He, H. Tang, *et al.*, "Non-diffracting light wave: fundamentals and biomedical applications," Front. Phys. **9**, 698343 (2021).
6. X. Ren, Q. Zhou, Z. Xu, *et al.*, "Particle trapping in arbitrary trajectories using first-order Bessel-like acoustic beams," Phys. Rev. Appl. **15**, 054041 (2021).
7. W. Hu, Z. Xu, H. Jiang, *et al.*, "Image restoration algorithm for terahertz FMCW radar imaging," Appl. Opt. **62**, 5399–5408 (2023).

Table 1. Comparison Related Reported Work of Metasurface Based Bessel Beam Array

Refs.	Beam Array Type	NA	Maximum Aspect Ratio	FWHM	Uniformity	Material of Metasurface
[20], 2017	1×1	0.9	10.0	135 nm, $\sim 0.3\lambda$	—	TiO_2 nanopillar on SiO_2
[25], 2020	2×2	0.2	9.09	590 nm, $\sim 0.5\lambda$	90.0%	TiO_2 nanopillar on SiO_2
[26], 2019	5×5	0.0195	5.63	1600 nm, $\sim 2\lambda$	42%	Si nanopillar on SiO_2
[27], 2022	4×4	0.4	3.75	570 nm, $\sim 0.9\lambda$	52%	Si nanopillar on SiO_2
This paper	4×4/irregular pattern	0.4/0.2	3.5	590 nm, $\sim 0.9\lambda$	69%/90%	Si nanopillar on SiO_2

8. H. Shi, H. Qi, G. Shen, *et al.*, "High-resolution underwater single-photon imaging with Bessel beam illumination," IEEE J. Sel. Top. Quantum Electron. **28**, 8300106 (2022).
9. R. Tudor, G. Bulzan, M. Kusko, *et al.*, "Multilevel spiral axicon for high-order Bessel–Gauss beams generation," Nanomaterials **13**, 579 (2023).
10. M. Baliyan and N. Nishchal, "Generating scalar and vector modes of Bessel beams utilizing holographic axicon phase with spatial light modulator," J. Opt. **25**, 095702 (2023).
11. C. Lutz, S. Schwarz, J. Marx, *et al.*, "Multi-Bessel beams generated by an axicon and a spatial light modulator for drilling applications," Photonics **10**, 413 (2023).
12. J. Wang, C. Cai, K. Wang, *et al.*, "Generation of Bessel beams via femtosecond direct laser writing 3D phase plates," Opt. Lett. **47**, 5766–5769 (2022).
13. X. Meng, X. Chen, R. Chen, *et al.*, "Generation of multiple high-order Bessel beams carrying different orbital-angular-momentum modes through an anisotropic holographic impedance metasurface," Phys. Rev. Appl. **16**, 044063 (2021).
14. L. Mohapi, L. M. Geiger, J. G. Korvink, *et al.*, "Simulating multilevel diffractive optical elements on a spatial light modulator," Appl. Opt. **61**, 7625–7631 (2022).
15. Z. Zhai, Z. Cheng, Q. Lv, *et al.*, "Tunable axicons generated by spatial light modulator with high-level phase computer-generated holograms," Appl. Sci. **10**, 5127 (2020).
16. L. Zhu, J. Yu, D. Zhang, *et al.*, "Multifocal spot array generated by fractional Talbot effect phase-only modulation," Opt. Express **22**, 9798–9808 (2014).
17. E. Tseng, S. Colburn, J. Whitehead, *et al.*, "Neural nano-optics for high-quality thin lens imaging," Nat. Commun. **12**, 6493 (2021).
18. A. H. Dorrah, N. A. Rubin, A. Zaidi, *et al.*, "Metasurface optics for on-demand polarization transformations along the optical path," Nat. Photonics **15**, 287–296 (2021).
19. X. Y. Fang, H. R. Ren, and M. Gu, "Orbital angular momentum holography for high-security encryption," Nat Photonics **14**, 102–108 (2020).
20. W. T. Chen, M. Khorasaninejad, A. Y. Zhu, *et al.*, "Generation of wavelength-independent subwavelength Bessel beams using metasurfaces," Light Sci. Appl. **6**, e16259 (2017).
21. Z. Wang, S. Dong, W. Luo, *et al.*, "High-efficiency generation of Bessel beams with transmissive metasurfaces," Appl. Phys. Lett. **112**, 191901 (2018).
22. S. Dong, Z. Wang, H. Guo, *et al.*, "Dielectric meta-walls for surface plasmon focusing and Bessel beam generation," Europhys. Lett. **122**, 67002 (2018).
23. F. Aieta, P. Genevet, M. A. Kats, *et al.*, "Aberration-free ultrathin flat lenses and axicons at telecom wavelengths based on plasmonic metasurfaces," Nano Lett. **12**, 4932–4936 (2012).
24. X. Li, M. Pu, Z. Zhao, *et al.*, "Catenary nanostructures as compact Bessel beam generators," Sci. Rep. **6**, 20524 (2016).
25. C. Chen, Y. Wang, M. Jiang, *et al.*, "Parallel polarization illumination with a multifocal axicon metalens for improved polarization imaging," Nano Lett. **20**, 5428–5434 (2020).
26. Z. Lin, X. Li, R. Zhao, *et al.*, "High-efficiency Bessel beam array generation by Huygens metasurfaces," Nanophotonics **8**, 1079–1085 (2019).
27. L. Chen, S. Kanwal, B. Yu, *et al.*, "Generation of high-uniformity and high-resolution Bessel beam arrays through all-dielectric metasurfaces," Nanophotonics **11**, 967–977 (2022).
28. R. W. Gerchberg and W. O. Saxton, "A practical algorithm for the determination of the phase from image and diffraction plane pictures," Optik **35**, 237–246 (1972).
29. J. A. Tropp and A. C. Gilbert, "Signal recovery from random measurements via orthogonal matching pursuit," IEEE Trans. Inf. Theory **53**, 4655–4666 (2007).
30. A. Maleki, L. Anitori, Z. Yang, *et al.*, "Asymptotic analysis of complex LASSO via complex approximate message passing (CAMP)," IEEE Trans. Inf. Theory **59**, 4290–4380 (2013).
31. C. Zhou and L. Liu, "Numerical study of Dammann array illuminators," Appl. Opt. **34**, 5961–5969 (1995).
32. Q. Wang, P. Ni, and Y. Xie, "On chip generation of structured light based on metasurface optoelectronic integration," Laser Photon. Rev. **15**, 2000385 (2021).
33. M. V. Berry, "The adiabatic phase and Pancharatnam's phase for polarized light," J. Mod. Opt. **34**, 1401–1407 (1987).